The response of relative humidity to centennial-scale warming over the southeastern Tibetan Plateau inferred from tree-ring width chronologies

Chunming Shi, Valérie Daux, Zongshan Li, Xiuchen Wu, Tianyi Fan, Qian Ma, Xiaoxu Wu, Huaiyu Tian, Matthieu Carré, Duoying Ji, et al.

The response of relative humidity to centennial-scale warming over the southeastern Tibetan Plateau inferred from tree-ring width chronologies

Chunming Shi[a], Valérie Daux[bf], Zongshan Li[c*], Xiuchen Wu[d], Tianyi Fan[a], Qian Ma[a], Xiaoxu Wu[a], Huaiyu Tian[a], Matthieu Carré[e], Duoying Ji[a], Wenli Wang[a], Annette Rinke[ag], Wei Gong[dh], Yan Liu[a], Yating Chen[a], Valérie Masson-Delmotte[b]

[a]College of Global Change and Earth System Science, Joint Center of Global Change and Green China Development, Beijing Normal University, Beijing 100875, China

[b]Laboratoire des Sciences du Climat et de l'Environnement (UMR CEA-CNRS-UVSQ 8212, Institut Pierre Simon Laplace, Gif-sur-Yvette, France)

[c]State Key Laboratory of Urban and Regional Ecology, Research Center for Eco-Environmental Sciences, Chinese Academy of Sciences, Beijing 100085, China

[d]State Key Laboratory of Earth Surface Processes and Resource Ecology, Faculty of Geographical Science, Beijing Normal University, Beijing 100875, China

[e]UM2-CNRS-IRD, Institut des Sciences de l'Evolution de Montpellier, Université Montpellier 2, CC065, Pl. Eugène Bataillon, 34095 Montpellier, France

[f]Université de Versailles - Saint Quentin, Versailles, France

[g]Alfred Wegener Institute Helmholtz Centre for Polar and Marine Research, Potsdam, Germany

[h]Institute of Land Surface System and Sustainable Development, Faculty of Geographical Science, Beijing Normal University, Beijing 100875, China

Corresponding author: Zongshan Li

Email: zsli_st@rcees.ac.cn; chunming.shi@bnu.edu.cn

Tel: +86-10- 62849803

Abstract

Understanding the past variability in atmospheric moisture associated with global warming is essential for reducing the uncertainties in climate projections. Such understanding is especially necessary in the Asian monsoon region in the context of increasing anthropogenic forcing. Here, we average four tree-ring width chronologies from the southeastern Tibetan Plateau (TP) over their common intervals and reconstruct the variability in regional relative humidity (RH) from the previous May to the current March over 1751-2005. In contrast to the summer drying associated with centennial-scale warming and the weakening of the Asian summer monsoon, our RH reconstruction shows no significant centennial trend from the 1820s through the 2000s. This absence of a consistent signal is due to the combined effects of contrasting moisture trends during the monsoonal and non-monsoonal seasons, which are controlled by summer monsoon precipitation and local convective precipitation, respectively. The interannual and decadal variability of our RH reconstruction is modulated by El Niño-Southern Oscillation (ENSO) and the Pacific Decadal Oscillation (PDO); however, these links are unstable over time. Two rapid increases in moisture are found to have occurred around the 1820s and 1980s; the latter increase caused the variability in RH during the 1980s-2000s to be the largest over the entire reconstruction period.

1 Introduction

Water vapor is the dominant greenhouse gas in the atmosphere and is associated with a significant positive feedback on global warming, which constitutes a key uncertainty in temperature projections (Hall and Manabe 1999; Held and Soden 2000; Held and Soden 2006). Both modelling and observational evidence show that global warming has increased atmospheric water vapor (here defined as specific humidity, SH) (Held and Soden 2000; Dai 2006; Sherwood and Meyer 2006), leading to intensification of the global water cycle and precipitation (Huntington 2006; Wentz et al. 2007; Zhang et al. 2007; Durack et al. 2012). A fixed relative humidity (RH) is usually assumed when modelling atmospheric SH changes (Held and Soden 2000). However, both instrumental data and Coupled Model Intercomparison Project Phase 5 (CMIP5) projections indicate that the variability in RH will be region-specific under warmer climate conditions (Dai 2006; Sherwood and Meyer 2006; Sherwood et al. 2010).

RH is an essential factor that modulates local hydrological and radiative processes by determining the degree of cloud cover and convective precipitation, as well as the rate of precipitation (Sherwood et al. 2010). In plant physiological models, RH is also used to approximate the water vapor deficit, a key factor that dominates stomatal conductance, the rate of photosynthesis and net primary production (NPP). The

simulated RH changes in response to anthropogenic forcing depend strongly on the horizontal resolution and the ability to resolve moisture transport of the model used (Sherwood et al. 2010). To date, inconsistent model outputs have been obtained, especially over land (Laine et al. 2014), and large discrepancies between models and observations still exist (Sabeerali et al. 2015). During the monsoon season over Asia, increases and decreases in RH in tropical India and southeastern China are projected by CMIP5 models, respectively (Laine et al. 2014). In contrast, on the Tibetan Plateau (TP), especially the southeastern TP, the RH trends projected by the CMIP5 models are quite ambiguous, and robust conclusions cannot be drawn from these model results (Duan et al. 2013; Laine et al. 2014). Instrumental observations show that the rate of warming over the TP is higher than that of the Northern Hemisphere and other regions at the same latitude, and this fast warming is especially pronounced after the 1980s (Qin et al. 2009; Duan and Xiao 2015). This warming trend has resulted in overall increases in RH and specific humidity (SH) on the TP (Kang et al. 2010; Yang et al. 2014). At the centennial scale, the responses of annual RH to the global warming that has occurred since the Industrial Revolution and the earlier warming that has occurred over the TP and the globe as a whole since the 1820s (Shi et al. 2015; Abram et al. 2016; Wilson et al. 2016) are still unclear.

The short and sparse instrumental observations over the TP are

93 inadequate to capture the variability in RH on multi-decadal to centennial
94 time scales. Therefore, paleoclimate proxies are increasingly used to
95 reconstruct past moisture variability around the world (Chapter 5 in IPCC
96 AR5, WG1, 2013) and Asia (Cook et al. 2010). Reconstructions using
97 snow accumulation, glacial varves and tree-ring $\delta^{18}O$ values all indicate
98 summer drying trends in the last century. These trends are associated with
99 reductions in precipitation, RH, and cloud cover over the central, southern
100 and southeastern TP (Shi et al. 2012; Liu et al. 2013; An et al. 2014;
101 Wernicke et al. 2015; Wernicke et al. 2017). These results are consistent
102 with the projected weakening of the Asian summer monsoon in response
103 to climate warming (Sabade et al. 2011; Sun and Ding 2011; Xu et al. 2012;
104 Sooraj et al. 2015). However, these centennial drying tends have not been
105 identified in reconstructions of total annual precipitation over the south-
106 central, southwestern and northern TP (Liu et al. 2011; Yang et al. 2014;
107 Liu and Nina 2015). Due to the lack of annual mean moisture
108 reconstructions, our understanding of past moisture variability is still
109 limited over the southeastern TP.

110 Within the southeastern portion of the TP, the radial growth of trees at
111 elevations of 3200-3500 m a.s.l. is controlled by temperature and
112 precipitation (Fan et al. 2009). Parameters that integrate both signals, e.g.,
113 the self-calibrating Palmer Drought Severity Index (scPDSI), are
114 commonly used as reconstruction targets (Fan et al. 2008; Fang et al. 2010;

Bi et al. 2015; Li et al. 2017). Therefore, these reconstructions cannot be used to disentangle the variations in temperature and moisture. Moreover, most previous studies have applied conservative detrending methods in processing tree-ring width (TRW) data. Compared with regional curve standardization (RCS), conservative detrending removes both age-related and climatic long-term trends, inherently leading to flat reconstructions without centennial trends (Esper et al. 2003). Thus, tree-ring reconstructions developed using sampling strategies that are designed specifically to target moisture variability and improved detrending methods are needed to understand the history of moisture conditions over the southeastern TP.

In this study, we sampled tree rings from 4 sites across the southeastern margin of the TP at elevations lower than those examined by previous studies. Signal-free RCS was applied to remove the non-climate signals and build standard TRW chronologies. This method preserves the signals of long-term climate and simultaneously avoids “end distortion” effects (Melvin and Briffa 2008). The common intervals of the Z-score standardized chronologies are averaged into a regional chronology and calibrated to instrumental RH measurements. Given the robust coherence between this chronology and the instrumental data, a regional RH reconstruction is produced. The RH reconstruction is analysed in terms of trends and regime shifts and compared with reconstructions of RH, the

scPDSI and temperature from nearby areas. The effects of large-scale climate variability over the Pacific Ocean on the regional RH are also analysed and discussed.

2 Materials and methods

2.1 Study area and meteorological data

Our study region is the northwestern Yunnan Province, which is located on the southeastern margin of the Tibetan Plateau and is the frontier of the summer Asian monsoon into the TP. The elevation of the study region ranges from 1000 m to 6740 m a.s.l. (**Fig. 1**). Land surface meteorological data (maximum temperature, precipitation, and RH) were obtained from two weather stations located at Weixi (2326 m a.s.l.) and Gongshan (1583 m a.s.l.) (**Fig. 1**). These stations have been in operation since 1955 and 1958, respectively. The meteorological data recorded at these 2 stations are highly coherent, and the correlation coefficients for annual mean temperature, total precipitation and RH are 0.62, 0.79 and 0.83 (P<0.001 for all of these variables), respectively. Therefore, the averages of the data from the two stations are taken to represent the regional meteorological conditions. The regional annual mean temperature and total precipitation are 13°C and 1343 mm respectively (**Fig. 1**). The summer precipitation of this region is dominated by the South Asian summer monsoon and the East Asian summer monsoon (Wang and Linho 2002). The scPDSI values covering the period 1958-2005 at the relevant

grid points (extending from 27 to 28°N and from 98 to 101°E) within a globally gridded scPDSI database were extracted and averaged (Dai et al., 2004) to assess the effects of drought on tree growth. Regionally averaged specific humidity, monthly mean temperature and precipitation (27-28°N 98-101°E, 1973-2003) on the land surface were extracted from the HadCRU dataset to identify the factors that dominate the variability in SH. The soil moisture (covering the period between 1960 and 2005) at the sampling sites is simulated using the Community Land Model 4.5 (CLM 4.5). To determine the connection between tree growth and large-scale modes of climate variability, such as the Pacific Decadal Oscillation (PDO) and El Niño-Southern Oscillation (ENSO), monthly PDO index values based on the NOAA Extended Reconstructed Sea Surface Temperature (ERSST) dataset and HadISST1 NINO3 index values were downloaded from the NOAA website (http://www.cdc.noaa.gov/data/climateindices/List/).

2.2 Tree-ring sampling, processing and chronology construction

The tree-ring samples used in this study were extracted from *Tsuga dumosa* (D. Don) Eichler growing in the four counties of Xin Zhu (XZ), Fu Gong (FG), Bing Zhong Luo (BZL) and Ta Cheng (TC) at elevations ranging from 2612 to 2966 m a.s.l. **(Table 1**; red circles in **Fig. 1**). All of the sampling sites are remote from human settlements and display no clear evidence of human activity. *Tsuga dumosa* (D. Don) Eichler is the

dominant species below an elevation of 3000 m a.s.l. in northwestern Yunnan Province, and it usually grows in cool and shaded regions. At each site, 33−41 adult trees with straight stems and no signs of damage or internal rotting were selected from areas of open canopy. Two cores per tree were taken from opposite sides of the trees using an increment borer with an inner diameter of 5.14 mm. This process was repeated until at least two cores reached the pith of each tree.

The core samples were dried in air and polished with progressively finer sandpaper until the rings were clearly visible. Tree-ring width (TRW) data were obtained using a Lintab® system, which has a resolution of 0.01 mm, and cross-dated by visual inspection under a microscope. The cross-dating quality was checked using the COFECHA software package (Holmes 1983). Measurements of pairs of cores from the same tree are averaged.

To preserve the long-term climate signals, avoid the effects of "trend distortion" and remove non-climatic signals, the signal-free regional curve standardization (SF-RCS) method (Melvin and Briffa 2008) is applied using the Climatic Research Unit Standardization of Tree-ring data (CRUST) software package (Melvin and Briffa 2014a; b). The TRW series from the individual sites are aligned by biological age (with pith offsets estimated for all samples using the concentric circles method). A signal-free iteration procedure is applied to remove the common growth forcing;

thus, the curves used to detrend the TRW data are free of climate signals (Melvin and Briffa 2008). The ring measurements after signal-free iteration are divided by the smoothed RCS curve value of the same ring age to create a TRW index. The robust mean of all of the TRW indices from each site is defined as the standard chronology. Portions of chronologies with sample depths of less than five trees are truncated. The linear trends for 1820-2005 are calculated for all the chronologies, and the significance levels of the linear regressions are calculated using the F-test. The multidecadal variations in these chronologies are assessed using 30-year loess smoothing.

To ensure the spatial representativeness and quality of the reconstruction, only the common intervals of the chronologies are averaged and standardized using Z-scores to produce a regional chronology. The regional chronology is also calculated by pooling all of the tree-ring materials from the four sites; the TRW data are then detrended using SF-RCS, standardized using Z-scores, and compared with the regional chronology derived using the first method.

2.3 Linear relationships between the TRW chronologies and the meteorological data

Correlation coefficients between the chronologies and monthly maximum temperatures, the scPDSI, precipitation, soil moisture and RH are calculated using the Dendroclim2002 software package (Biondi and

225 Waikul 2004) to identify the key climate factors that control tree growth
226 over the instrumental period (**Fig. 3**). The correlation is assessed over the
227 season extending from the previous March to the current September within
228 1959-2005 (1960-2005 for soil moisture).

229 **2.4 Regional climate reconstruction and error calculation**

230 A linear calibration model is used to reconstruct the climate proxy
231 (Fritts 1976), and leave-one-out cross-validation is conducted to test the
232 validity of the model (Michaelsen 1988). The reconstruction errors are
233 calculated as follows. The instrumental RH data and the regional
234 chronology are randomly divided into two halves. Each half is used to
235 calculate a linear calibration model that is validated using the other half,
236 yielding 47 error values. The 2.5% and 97.5% percentiles of the error
237 population after 1,000 iterations are defined as the bounds of the 95%
238 confidence interval of the RH reconstruction.

239 **2.5 Regime shift analysis**

240 To test the shift in the mean value, a regime shift analysis is conducted
241 using a moving window of 30 years in the Regime Shift Detection software
242 package, v3.2 (Rodionov, 2004).

243 **3 Results**

244 **3.1 Chronologies and trends**

245 Principal component analysis of the Z-score standardized TRW
246 chronologies (black lines in **Fig. 2a–d**) shows that the leading principal

247 component explains 47% of the total variance, suggesting a strong
248 common signal among the chronologies. The regional chronologies
249 derived using the two methods described in the Methods section are highly
250 correlated (R=0.91, P<0.001; black and blue lines in **Fig. 2e**), and the
251 average of the four chronologies is defined as the regional chronology.

252 The TC and FG chronologies show slight but significant (P<0.05)
253 increasing and decreasing trends, respectively (**Fig. 2a and 2c**
254 respectively). The BZL and XZ chronologies show no statistically
255 significant trends (**Fig. 2b and 2d** respectively). The 25-year moving
256 expressed population signal (EPS) calculated for each chronology is
257 generally above 0.85 (horizontal red lines in **Fig. 2a-2d**).

258 **3.2 Correlations between TRW chronologies and meteorological data**

259 Monthly maximum temperature shows an overall negative effect on
260 tree growth; however, this effect is insignificant (**Fig. 3a**). The TRW
261 chronologies generally show insignificant correlations with the scPDSI,
262 precipitation and soil moisture in most months (**Fig. 3b, 3c and 3d**).
263 Significant correlation with the scPDSI can only be found in the previous
264 October for BZL and XZ (**Fig. 3b**). Only TC and XZ are significantly
265 correlated with precipitation during the current January (**Fig. 3c**). Despite
266 their statistically insignificant effects on most chronologies, the positive
267 effect of the scPDSI and soil moisture on tree growth is observed for a
268 consecutive period that extends from the previous to the current year (**Fig.**

3b and 3d).

The highest correlation coefficients are obtained between the chronologies and monthly mean RH from the previous May to the current March (pMay-cMar) (**Fig. 3e**). For the regional chronology, the correlation coefficients are significant at the 95% level from pMay to cMar, except for the previous September and November and the current March. The correlation coefficients describing the relationship between the pMay-cMar averaged RH and the individual/regional chronologies fall between 0.42 and 0.69, and these correlations are all significant at the 99% confidence level (R^2=0.48, P<0.001 for the regional chronology) (**Fig. 3e**).

3.3 Regional relative humidity reconstruction

Based on the high correlation coefficients between the regional chronology and the instrumental RH (R^2=0.48, P<0.001, n=47; **Fig. 3e**), a linear calibration model is used to reconstruct the past RH averaged from the previous May to the current March. Specifically, $RH_{pMay-cMar}$=1.55×chronology+73.53 (in %). The values of the reduction of error (RE) statistic and the coefficient of efficiency (CE) and the results of the product means test (PMT) and the sign test (ST) are 0.43, 0.42, 3.36 and 12.26 (P<0.001), respectively; thus, the linear calibration model is valid for RH reconstruction. Our $RH_{pMay-cMar}$ reconstruction is shown in **Fig. 4**; grey shading indicates the 95% confidence interval. The regime shift analysis demonstrates an abrupt shift towards a wetter state in 1825

(significant at the 99% level; thick black line in **Fig. 4**). The trends over 1820-2005 and 1850-2005 are statistically insignificant (slope=-0.0056± 0.02% and 0.0023 ± 0.003%, P=0.67 and 0.16, respectively), and the interannual amplitude is within ±2.55%. The greatest decadal variability is noted from the 1980s to the 2000s (red line in **Fig. 4**), and 2004-2005 is the wettest epoch seen in the entire reconstruction period; these features are the results of the rapid increase in $RH_{pMay\text{-}cMar}$ since the 1980s.

3.4 Coherence of instrumental and reconstructed RH with PDO and ENSO

We calculate the monthly correlation coefficients between the instrumental and reconstructed $RH_{pMay\text{-}cMar}$ records with the PDO and ENSO from 1959 to 2005, which is the period that common among all of the climate records except soil moisture (**Fig. 5)**. The instrumental and reconstructed $RH_{pMay\text{-}cMar}$ are both significantly (P<0.05) and negatively correlated with the PDO index value of the previous year (January-March and February-April, respectively). The instrumental $RH_{pMay\text{-}cMar}$ is negatively correlated with the NINO3 index from the previous January to June, but this correlation does not reach the 95% significance level. On the other hand, the $RH_{pMay\text{-}cMar}$ reconstruction is significantly and negatively correlated with the NINO3 index from the previous January to April.

4 Discussion

4.1 Climatic effects on tree growth in the study region

313 The growth of trees at low elevations generally lack positive
314 temperature signals (Fritts 1976). The mean elevation of our sampling sites
315 is 2738 m a.s.l., which is much lower than those of nearby alpine treelines
316 with elevations of 3522-4221 m a.s.l. (Shi et al. 2015) and is also lower
317 than the nearby sites where a scPDSI reconstruction was obtained (mean
318 elevation 3050 m a.s.l.) (Fang et al. 2010). Thus, our chronologies show
319 insignificant correlation with temperature (**Fig. 3a**). Given that
320 precipitation is abundant (1343 mm/year; **Fig. 1**), the tree growth is
321 unlikely to have been limited by moisture availability, as represented by
322 precipitation, the scPDSI and soil moisture (**Fig. 3b, 3c, 3d**). RH is closely
323 linked with the atmospheric vapor pressure deficit. Low values of RH (i.e.,
324 high vapor pressure deficits) are usually accompanied by low stomatal
325 conductance and even stomatal closure, leading to decreased fluxes of CO_2
326 into leaves and photosynthetic rates (Oren et al. 1999; Flexas and Medrano
327 2002; Lawlor and Cornic 2002). The limiting effect of water vapor deficits
328 on tree growth is prominent for needle-leaf tree species, such as *Pinus*
329 *taeda* and ponderosa pine (Ewers and Oren 2000; Ryan et al. 2000). We
330 suggest that, in this study, the xylogenesis associated with tree growth is
331 limited by the connection between photosynthetic rates and RH.
332 Significant correlations between tree growth and RH in the previous
333 seasons (**Fig. 3e**) and high one-year-lag autocorrelation coefficients (AC1,
334 0.70-0.87) (**Table 1**) have also been reported from nearby regions (Fang et

al. 2010). These observations suggest the existence of a “storage” or “memory” effect for this evergreen tree species: photosynthetic products generated prior to the current growing season (including the previous winter) are stored and used for xylogenesis during the following year (Fritts 1976).

4.2 Coherence of the $RH_{pMay\text{-}cMar}$ reconstruction and PDO/ENSO at interannual to decadal scales

The PDO is a long-lived El Niño-like pattern of climate variability. A robust inverse relationship between the Asian summer monsoon (ASM) and the PDO during the last century has been identified (Krishnan and Sugi 2003; Krishnamurthy and Krishnamurthy 2014a). Superimposed on this decadal variability, ENSO also has a significant effect on ASM intensity, mainly at interannual scales (Krishnamurthy and Goswami 2000; Krishnamurthy and Krishnamurthy 2014b). Fang et al. (2010) indicates that the annual mean precipitation and the scPDSI values in a nearby region (blue circles in **Fig. 1**) are modulated by the PDO and ENSO. Similarly, we find significant negative correlations between the instrumental and reconstructed $RH_{pMay\text{-}cMar}$ with the PDO and ENSO indices. Both studies confirm that the effects of the PDO and ENSO are not confined to the monsoon season.

To test the decadal coherence of $RH_{pMay\text{-}cMar}$ and the PDO, both series

are smoothed using 30-year loess functions and are shown in **Fig. 6a**. $RH_{pMay\text{-}cMar}$ appears be anti-phased coherent with January-to-April average PDO index values in the post-1960s period (**Fig. 6a**), as is confirmed by wavelet coherence analysis (**Supplementary Fig. 1)**. From the 1900s to the 1960s, the coherent pattern appears to be positive (**Fig. 6a**), but wavelet coherence analysis suggests that it is statistically insignificant (**Supplementary Fig. 1)**. The correlation and coherence analysis in this study demonstrate that ENSO and the PDO modulate $RH_{pMay\text{-}cMar}$ at interannual to decadal time scales. Unstable relationships between PDO/ENSO and moisture variability on the TP have been reported by previous study (Shi et al. 2010).

4.3 Centennial variability in RH and underlying mechanisms

A persistent warming trend since the 1820s has been detected over Asia as a whole (PAGES 2k Consortium 2013). Of the 229 chronologies used in the Asian PAGES 2K project, 98 are from the TP (defined as the region bounded by 27-38°N and 75-103°E). The early onset of global warming from the 1820s has been confirmed by recent studies (Abram et al. 2016; Wilson et al. 2016). Based on seven alpine treeline chronologies, Shi et al. (2014) reported that the summer temperatures in a nearby region (28-33°N 98-103°E) has increased since the 1820s (**Fig. 6b**). The ASM is weakening in response to the centennial-scale warming because the rate of increase in surface temperatures over the subtropical oceans around Asia

is faster than that over land, and the land-ocean thermal contrast is decreasing (Sun and Ding 2011; Turner and Annamalai 2012; Xu et al. 2012). The weakening ASM and the corresponding decrease in summer RH are evident over the monsoonal TP, i.e., the region between the Tanggula and Himalayan Mountains, as defined by Tian et al. (2001), in the last century (Liu et al. 2013; An et al. 2014; Wernicke et al. 2015; Wernicke et al. 2017). On the other hand, during the non-monsoon season on the southeastern TP, a warm-wet association has been reported for the last several centuries (Li et al. 2017). In the northern (non-monsoonal) TP, where precipitation is controlled by the westerlies, annual precipitation has been found to have increased since the mid-19th century (Yang et al. 2014). Both cases of increased moisture are due to anomalously high evaporation, SH, and local convective precipitation caused by concurrent warming (Yang et al. 2014; Li et al. 2017). The increase in atmospheric SH is the largest positive feedback that drives warming and is the main reason for projections of increased precipitation at middle and high latitudes in model simulations (Dai 2006).

In our study region, which receives abundant annual precipitation and displays large variability in the summer monsoon, we assume that different mechanisms that drive SH contribute to the contrasting RH trends in the monsoonal and non-monsoonal seasons. We test this assumption by examining the SH values during the monsoon (June-August, JJA) and non-

monsoon seasons (from the previous September to the current May) with the concurrent temperature and precipitation averaged over the sampling region (27-28°N, 98-101°E; 1973-2003). The non-monsoonal SH is significantly correlated with the concurrent temperature (R=0.57, P<0.001; **Fig. 7a**) and does not display a significant correlation with precipitation (R=0.19, P=0.31; **Fig. 7b**). The abundant precipitation (1343 mm/year) may well have supported the increase in SH with warming during the non-monsoon season over the last several decades, which is an unprecedentedly warm period over the last few centuries (Liang et al. 2009; Liu et al. 2009; Wang et al. 2014; Shi et al. 2015; Wang et al. 2015). In contrast, the SH of the monsoon season is insensitive to temperature variability (R=0.18, P=0.32; **Fig. 7c**) but is significantly correlated with precipitation amount during the monsoon season (R=0.56, P<0.001; **Fig. 7d**). The coherence of SH and precipitation during the monsoon season suggests that the summer moisture is controlled by the ASM circulation pattern.

RH is usually calculated as the ratio of SH to saturated SH; the latter quantity increases with temperature. Therefore, a temperature-insensitive SH will lead to a minor decrease in RH during the monsoon season (statistically insignificant; black line in **Supplementary Fig. 2**). On the other hand, $RH_{pMay\text{-}cMar}$, which is mainly dominated by the non-monsoonal RH (blue and red lines in **Supplementary Fig. 2**), shows a significant increasing trend over the instrumental period; the most prominent tend

appears after the 1980s. The opposite trends in RH in the monsoonal and non-monsoonal seasons may represent one reason for the insignificant centennial trend in our $RH_{pMay\text{-}cMar}$ reconstruction. However, the interplay of RH between the monsoonal and non-monsoonal seasons over long time scales is still unclear, given that instrumental data are lacking in the past.

The long-term increases in CO_2 that have occurred since the Industrial Revolution, particularly the rapid increase in CO_2 over the last decades, could stimulate increased water use efficiency and tree growth of alpine treelines over the southeastern TP since the 1960s (Huang et al. 2017). However, the regional chronology of this study shows no persistent growth enhancement since the 1860s or 1960s (**Fig. 2e)**, and the inter-decadal variabilities of the instrumental and reconstructed RH are highly coherent in the last five decades (**Fig. 4)**, it seems the CO_2 fertilization effect is insignificant in this study.

4.4 Comparisons with nearby RH and the scPDSI reconstructions

The nearest RH reconstruction, which was published by An et al. (2014) (blue triangle in **Fig. 1**), is compared with our $RH_{pMay\text{-}cMar}$ record (**Fig. 6c)**. An et al. (2014) showed a persistent decrease in summer RH associated with centennial-scale warming and ASM weakening since the 1850s (Liu et al. 2013; An et al. 2014; Wernicke et al. 2015; Wernicke et al. 2017). Our $RH_{pMay\text{-}cMar}$ reconstruction lacks long-term trends and represents a combination of opposing moisture trends in the monsoon and

444 non-monsoon seasons with centennial-scale warming. Both our $RH_{pMay\text{-}cMar}$
445 record and the RH reconstruction of An et al. (2014) reflect wetting trends
446 in the 1770s through the 1840s (**Fig. 6c**). The abrupt increase in $RH_{pMay\text{-}}$
447 $_{cMar}$ in the 1820s coincides with the onset of significant warming over the
448 southeastern TP (**Fig. 6b**) (Shi et al. 2015), which may have produced
449 increases in SH in the non-monsoon season. In addition, this shift overlaps
450 with a period of elevated summer RH values on the southeastern TP that
451 occurred in the late 1810s. During this period, the ASM was recovering
452 from the previous dry conditions caused by the 1809 Unknown and 1816
453 Tambora volcanic eruptions (Shi et al. 2012). The most strongly
454 contrasting trends between An et al. (2014) and our reconstruction are
455 found in the 1980s-2000s, when an unprecedentedly rapid rate of warming
456 is reported over the southeastern TP (**Fig. 6b**) (Shi et al. 2015). The
457 negative PDO phase and the increased non-monsoon season SH associated
458 with the rapid warming could both have favoured the anomalously high
459 $RH_{pMay\text{-}cMar}$ of the last several decades (**Fig. 5, 6a and 7a**)

460 The 30-year smoothing of a nearby scPDSI reconstruction (blue
461 circles in **Fig. 1**; the annually resolved data have not yet been published)
462 that employs a similar seasonal extent (from the previous May to the
463 current April) shows no long-term trend or abrupt regime shift (Fang et al.
464 2010) and is coherent with our $RH_{pMay\text{-}cMar}$ reconstruction at the
465 multidecadal scale (**Fig. 6d**). These similarities may arise from a

significant correlation between the instrumental annual mean scPDSI and RH values within the sampling region (R=0.40, *P*=0.004; 1958-2005).

5 Conclusions

Our results show that atmospheric water vapor on the southeastern TP, specifically the SH during the monsoon and non-monsoon seasons, is controlled by ASM precipitation and local evaporation processes, respectively. Centennial-scale warming has weakened the ASM and decreased summer RH beginning in the mid-19th century on the southeastern TP. Given the abundant precipitation, the warming during the non-monsoon season has increased evaporation and SH. Because our $RH_{pMay\text{-}cMar}$ reconstruction represents the combined effects of contrasting moisture trends in the monsoon and non-monsoon seasons, it does not display a centennial trend from the 1820s through the 2000s, when significant warming prevailed over the southeastern TP. Two rapid increases in moisture are detected in the 1820s and 1980s. The former coincides with the onset of significant warming over the southeastern TP and overlaps with the recovery of the ASM from dry conditions caused by consecutive volcano eruptions. The latter is associated with rapid warming and increased SH during the non-monsoon season and may have been additionally enhanced by the negative phase of the PDO.

Acknowledgements: This study was supported by the National Natural Science Foundation of China (NSFC; 31600354), the National Research and Development Programme of China (2016YFC0502105), and the Fundamental Research Funds for the Central Universities.

Table and figure captions:

Tab. 1: Detailed information on the meteorological stations and sampling sites, as well as summary statistics of the chronologies.

Fig. 1: Sampling sites and climatic context of the study area.

Fig. 2: Standardized TRW chronologies and the regional composite of the 4 chronologies.

Fig. 3: Correlation coefficients between the TRW chronologies and the regional chronology with monthly climate indices.

Fig. 4: RH reconstruction with regime shift and linear trend analyses.

Fig. 5: Monthly correlation coefficients of instrumental and reconstructed RH values with the PDO and NINO3 indices.

Fig. 6: Comparison of our RH reconstruction with the PDO and climate reconstructions from nearby regions.

Fig. 7: Annual and summer mean SH and temperatures within the sampling region

Supplementary Fig. 1: Wavelet coherence analysis of RH reconstruction and the PDO.

Table 1: Latitude (Lat. N), longitude (Lon. E) and elevation (Elev.) of the sampling sites, a nearby tree-ring study (Fang et al. 2010) and meteorological stations; the species and number of successfully cross-dated trees at each site (N. tr.); the mean sensitivity (MS) and first order autocorrelation coefficient (AC1) of the chronologies; and the time spans covered by data from the weather stations and chronologies (Sta./Tr. Span).

Sites/Stations	Lat. N	Lon. E	Elev. (m)	N. tr.	MS	AC1	Species	Sta./Tr. Span
XZ	27.25	98.99	2966	41		0.87	*Tsuga dumosa*	1475-2005
FG	26.99	98.82	2731	37		0.77	*Tsuga dumosa*	1600-2005
BZL	28.00	98.61	2612	33		0.70	*Tsuga dumosa*	1744-2005
TC	27.39	99.34	2825	36		0.73	*Tsuga dumosa*	1751-2005
WXI	27.33	99.29	3060	24	0.23	0.85	*Abies forrestii*	1349-2007
WEX	27.31	99.30	3040	25	0.24	0.83	*Abies forrestii*	1348-2007
PTG	27.59	99.45	3050	15	0.22	0.82	*Abies forrestii*	1483-2007
Gongshan	27.45	98.40	1583					1958-2005
Weixi	27.10	99.17	2326					1955-2005

Figure 1: Sampling sites and study area. The right bottom insert shows the TP (grey shading indicates elevations above 3000 m) and the sampling region (black rectangle). The right top inset displays a Walter-Lieth diagram of the study region; the temperatures (black curve) and precipitation (grey bars) represent the average values from the Weixi and Gongshan meteorological stations (1959-2005). Within the sampling region (main figure), the filled red circles indicate our sampling sites (see Table 1 for details), whereas the filled triangles show the positions of nearby meteorological stations. The blue circles and triangle indicate the sampling sites of nearby reconstructions of the scPDSI and RH (An et al. 2014; Fang et al. 2010).

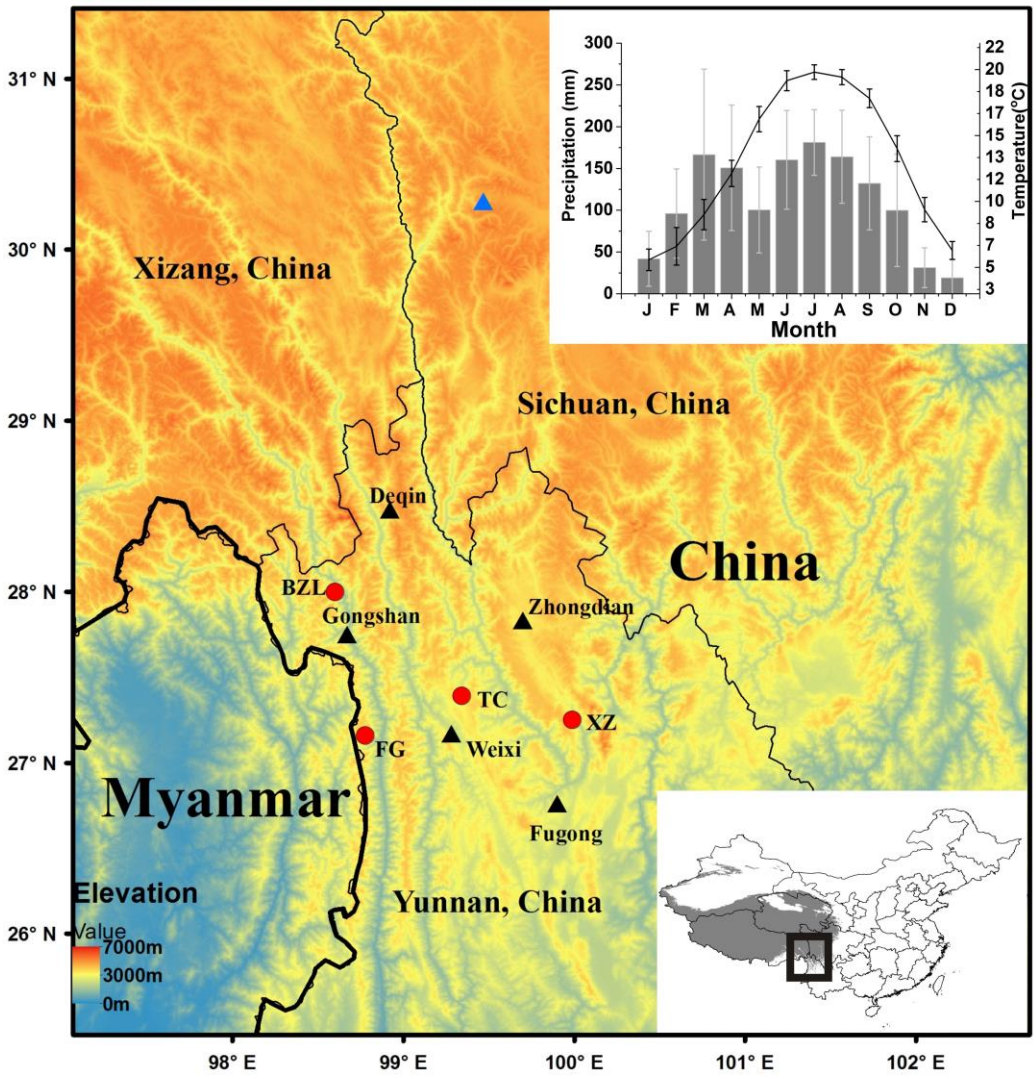

Figure 2: Z-score standardized TRW chronologies (a-d, SF-RCS detrended) and regional chronologies derived from the two methods (e). Thick red lines show the 30-year loess-smoothed chronologies. Thick black lines represent the linear trends calculated for each chronology from 1820 to 2005. Horizontal red lines represent the 25-year moving expressed population signal (EPS) value for each chronology (right-hand vertical axis).

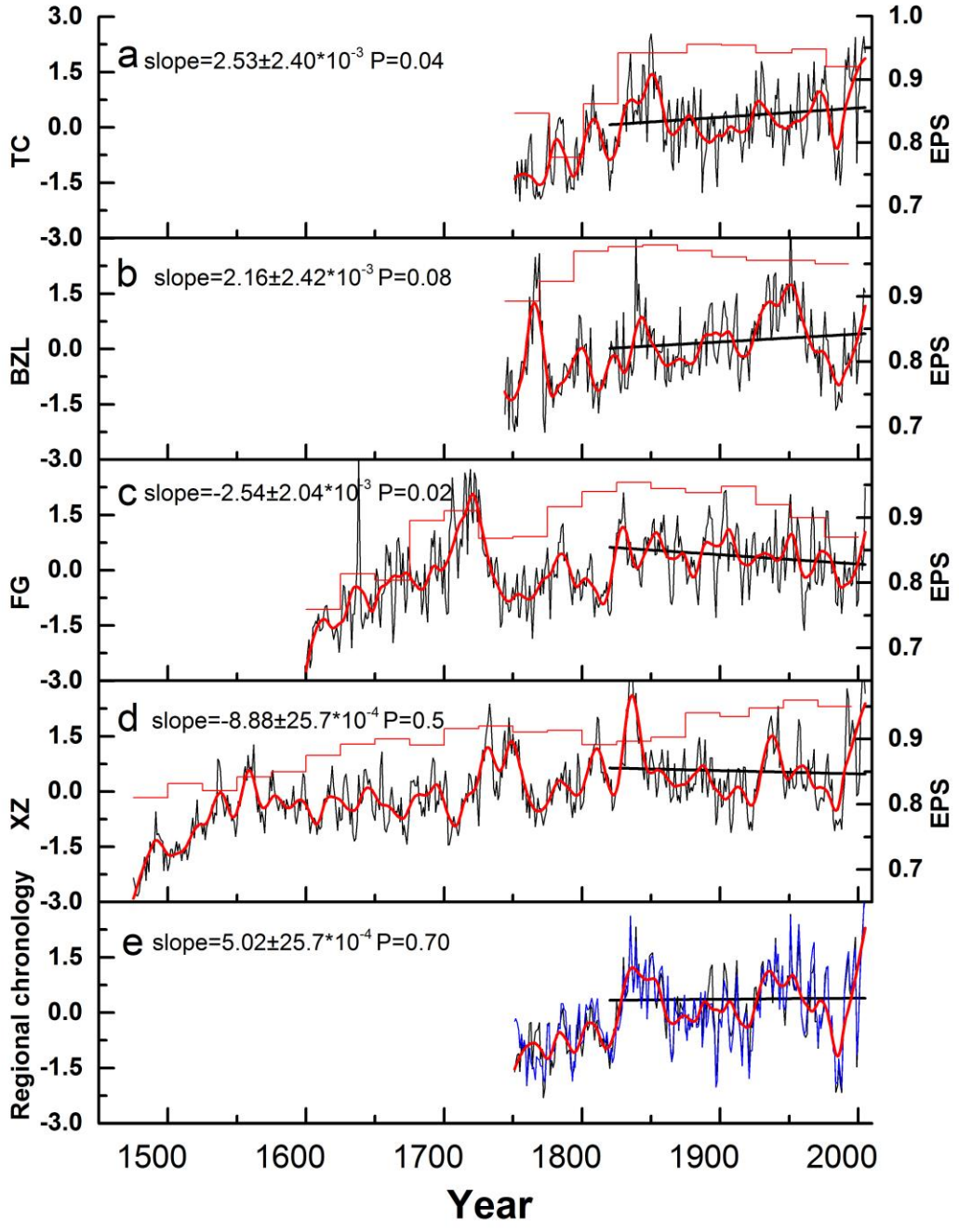

Figure 3: Correlation coefficients between the TRW chronologies and the regional chronology (Reg. Chro.) with the monthly regional meteorological data from May of the previous year to September of the current year. 3a: maximum temperature; 3b: the scPDSI; 3c: precipitation; 3d: soil moisture; 3e: RH. Correlation coefficients between the TRW chronologies and Reg. Chro. with RH averaged from the previous May to the current March (pMay-cMarch) are shown in 3e. Significance levels of 0.05, 0.01 and 0.001 are shown as dotted, dashed and solid lines, respectively.

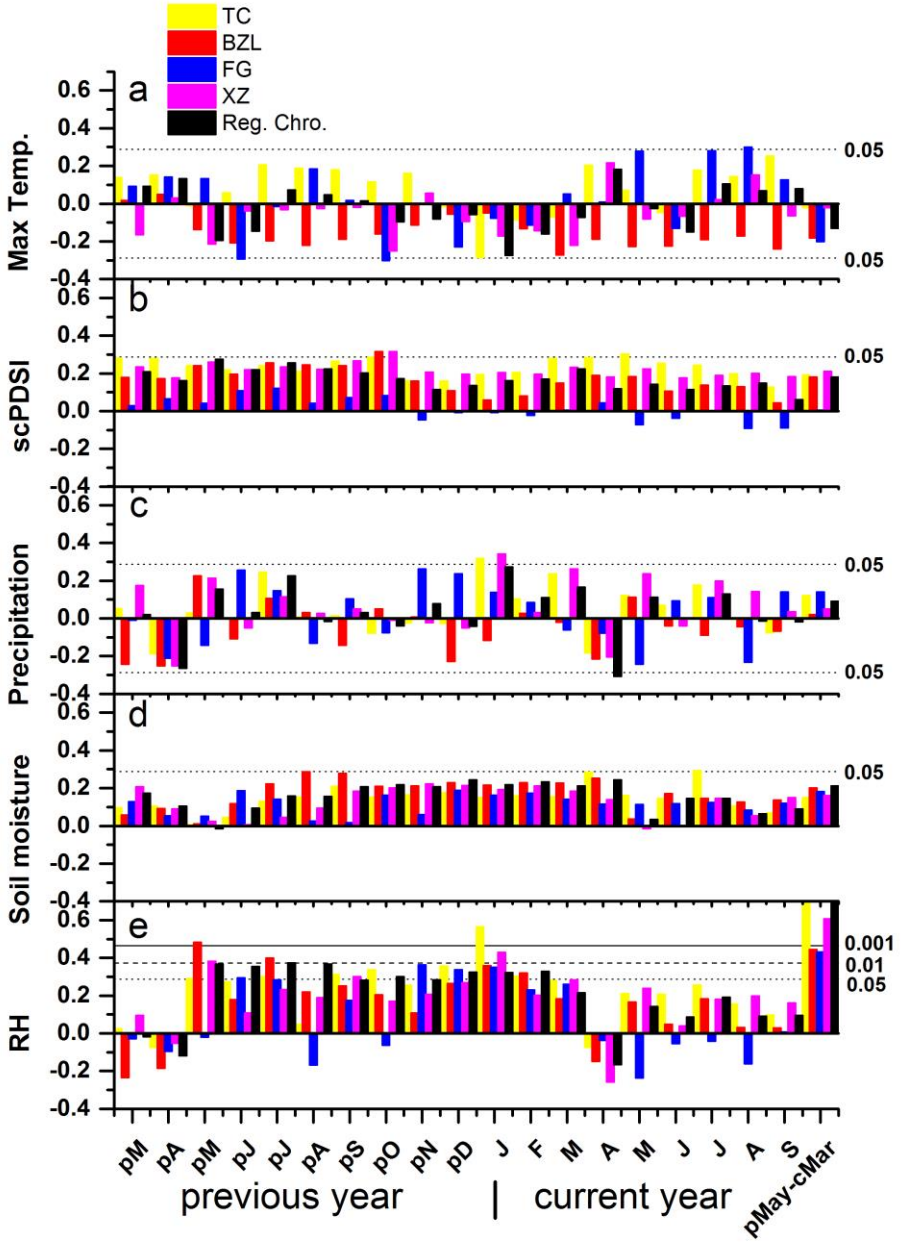

Figure 4: Relative humidity reconstruction (thin black line) and instrumental $RH_{pMay\text{-}cMar}$ (blue line); the 95% confidence interval of the reconstruction is indicated with grey shading. The thick black line shows a shift in the moving mean value (i.e., a regime shift; significant at the 95% level). Red and yellow lines represent the 30-year standard deviation and loess smoothing of the reconstruction, respectively.

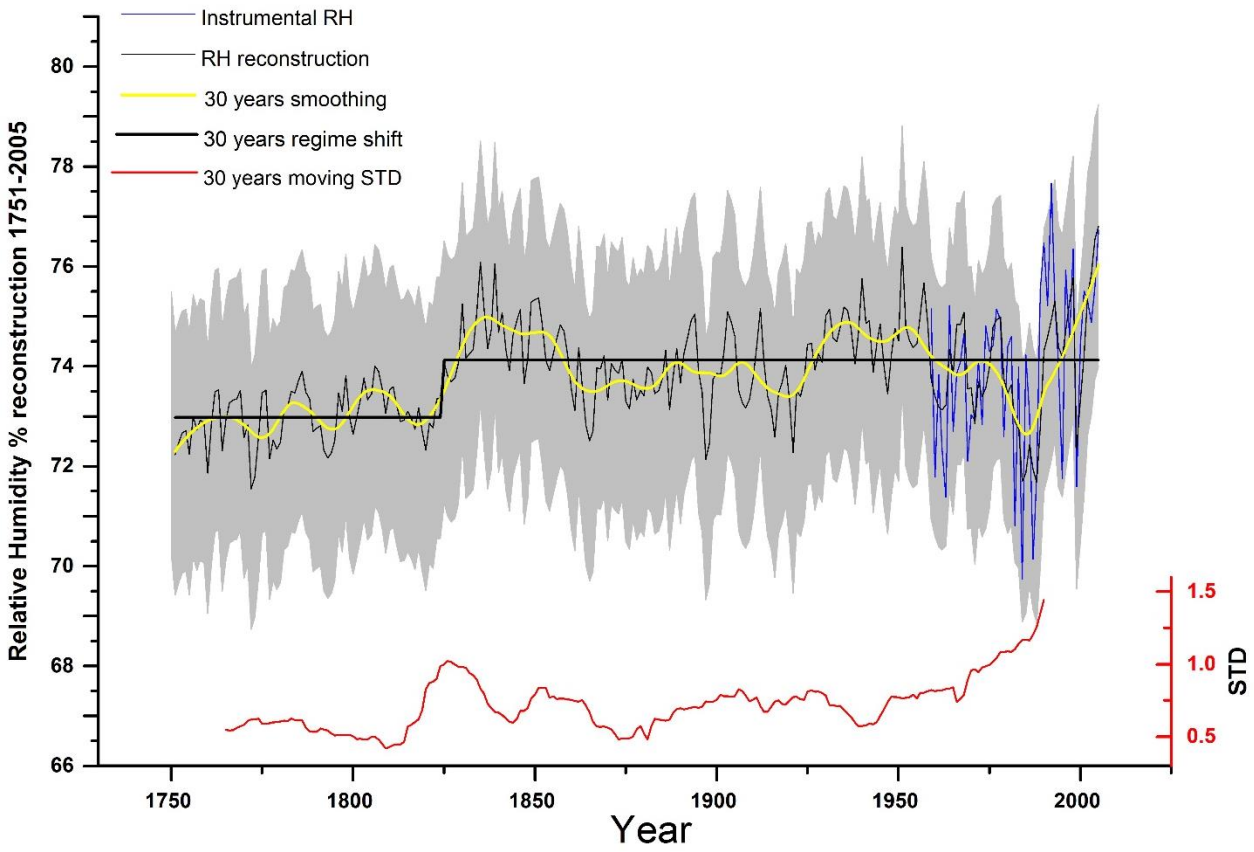

Figure 5: Monthly correlation coefficients of the instrumental and reconstructed $RH_{pMay\text{-}cMar}$ with the PDO and NINO3 indexes from the previous January to the current December. Significance levels of 95% and 99% are shown as dotted and solid lines.

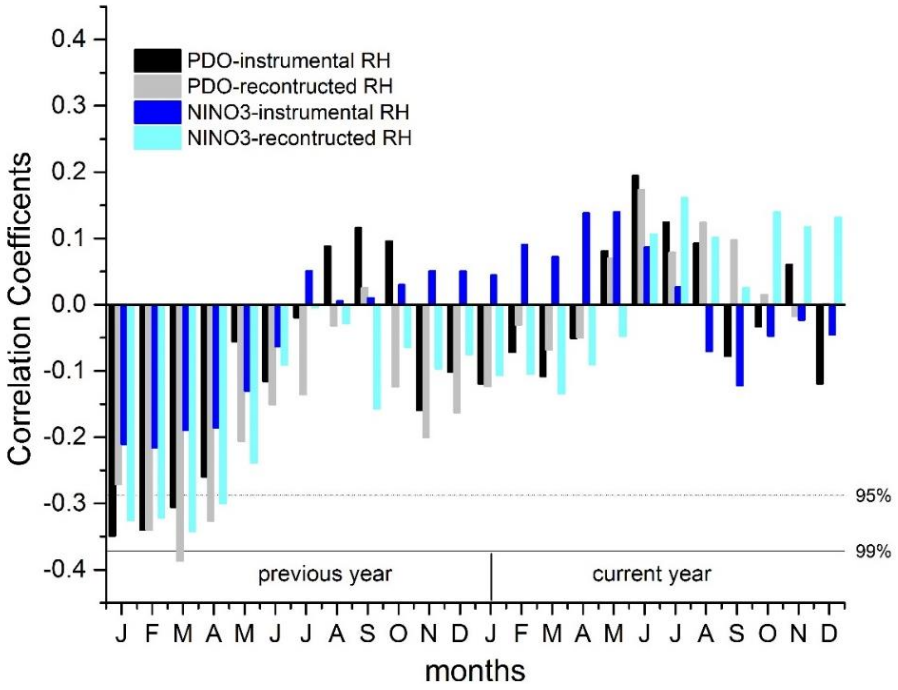

Figure 6: Comparison of our RH reconstruction (red line) with the PDO index and climate reconstructions from nearby regions. (a): Jan-Apr averaged PDO; (b): regional summer temperature reconstruction (N 28–33° E 98–103°) published by Shi et al. 2015; (c): summer RH reconstruction published by An et al. 2014 (blue triangle in **Fig. 1**); (d): annual scPDSI reconstruction published by Fang et al. 2010 (blue circles in **Fig. 1**). All data are normalized to 0-1 and smoothed with a 30-year loess function.

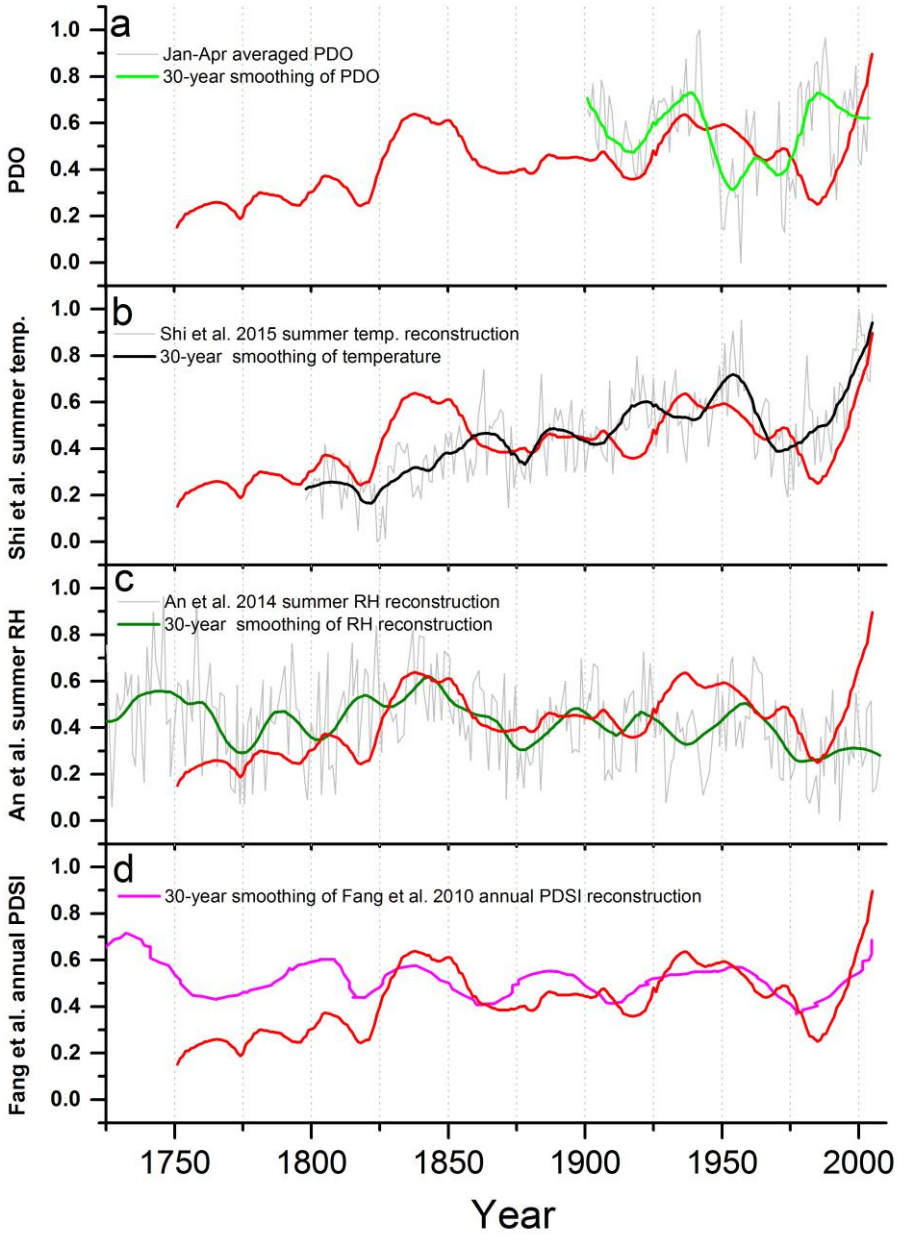

554 **Figure 7:** Correlation coefficients of the non-monsoonal and monsoonal (JJA) SH with the concurrent

555 temperature and precipitation within the study region.

556

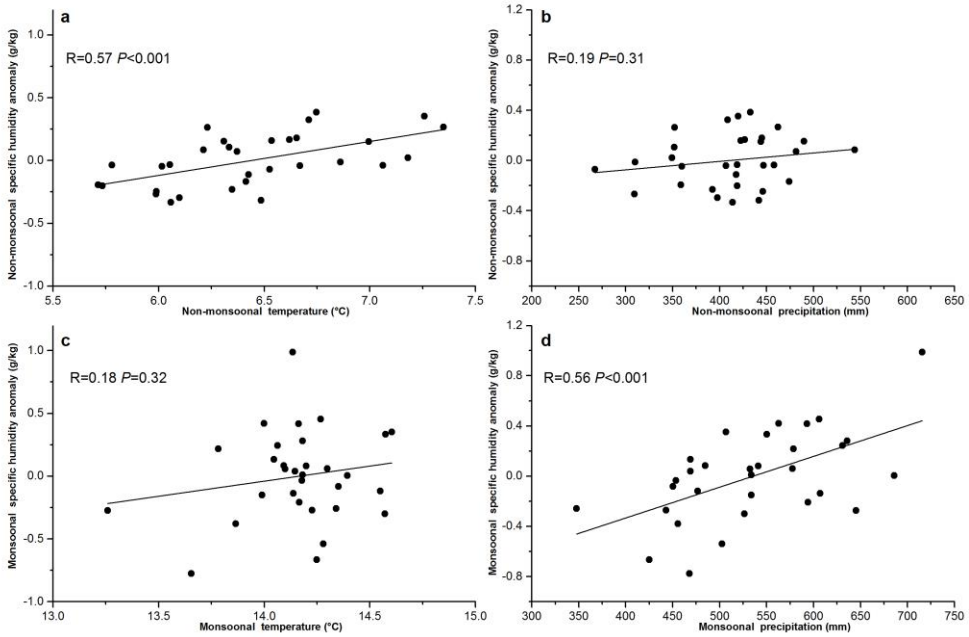

Supplementary Figure 1: Wavelet coherence analysis of the RH reconstruction and the January-to-April averaged PDO. Black symbols indicate significant coherence at the 95% level.

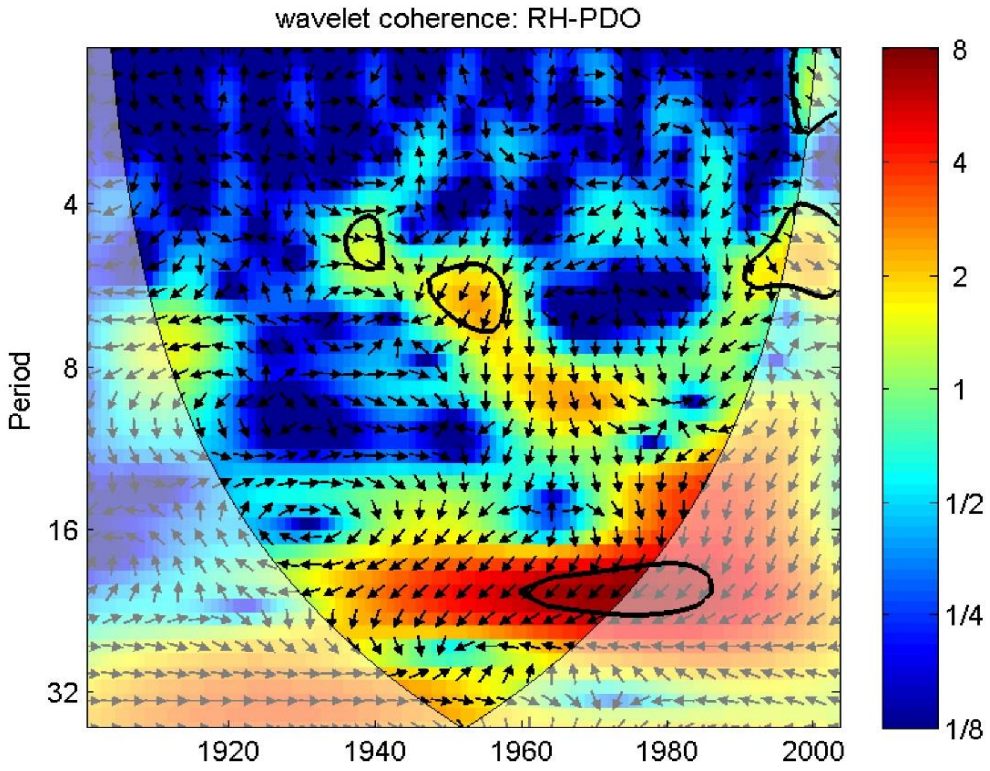

Supplementary Figure 1: Regional RH of the study region (average of Weixi and Gongshan stations). Black, blue and red lines indicate the monsoonal, pMay-pMar and non-monsoonal seasons.

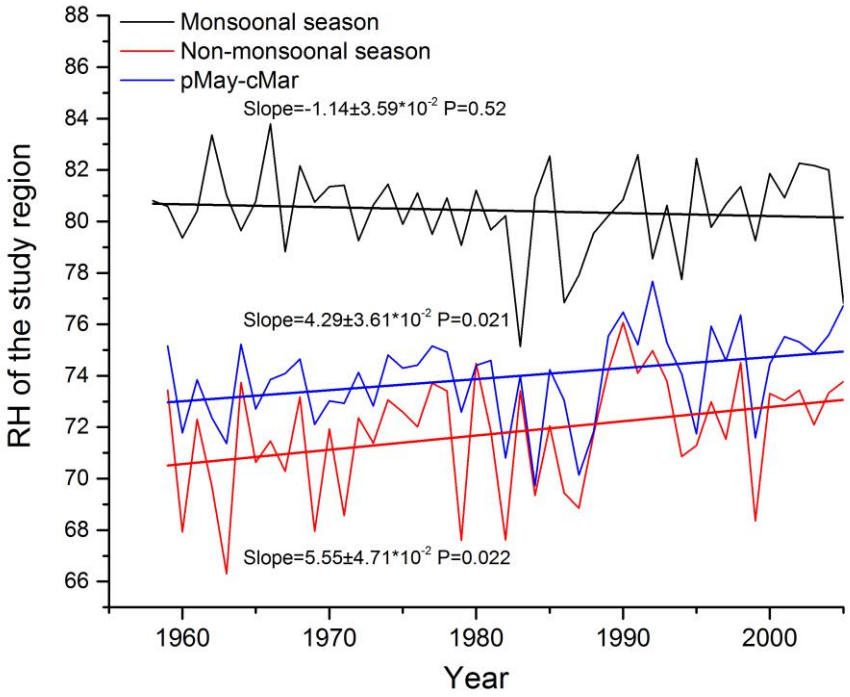

References:

Abram NJ, Mcgregor HV, Tierney JE, Evans MN, Mckay NP, Kaufman DS (2016) Early onset of industrial-era warming across the oceans and continents. Nature 536: 411

An W, Liu X, Leavitt SW, Xu G, Zeng X, Wang W, Qin D, Ren J (2014) Relative humidity history on the Batang-Litang Plateau of western China since 1755 reconstructed from tree-ring delta O-18 and delta D. Clim Dynam 42: 2639-2654

Bi Y, Xu J, Gebrekirstos A, Guo L, Zhao M, Liang E, Yang X (2015) Assessing drought variability since 1650 AD from tree-rings on the Jade Dragon Snow Mountain, southwest China. Int J Climatol 35: 4057-4065

Biondi F, Waikul K (2004) DENDROCLIM2002: A C++ program for statistical calibration of climate signals in tree-ring chronologies. Comput Geosci-Uk 30: 303-311

Cook ER, Anchukaitis KJ, Buckley BM, D'Arrigo RD, Jacoby GC, Wright WE (2010) Asian Monsoon Failure and Megadrought During the Last Millennium. Science 328: 486-489

Dai A (2006) Recent climatology, variability, and trends in global surface humidity. J Clim 19: 3589-3606

Duan A, Hu J, Xiao Z (2013) The Tibetan Plateau Summer Monsoon in the CMIP5 Simulations. J Clim 26: 7747-7766

Duan A, Xiao Z (2015) Does the climate warming hiatus exist over the Tibetan Plateau? Sci Rep-Uk 5

Durack PJ, Wijffels SE, Matear RJ (2012) Ocean Salinities Reveal Strong Global Water Cycle Intensification During 1950 to 2000. Science 336: 455-458

Esper J, Cook ER, Krusic PJ, Peters K, Schweingruber FH (2003) Tests of the RCS method for preserving low-frequency variability in long tree-ring chronologies. Tree-Ring Res 59: 81-98

Ewers BE, Oren R (2000) Analyses of assumptions and errors in the calculation of stomatal conductance from sap flux measurements. Tree Physiol 20: 579-589

Fan Z, Brauning A, Cao K (2008) Tree-ring based drought reconstruction in the central Hengduan Mountains region (China) since AD 1655. Int J Climatol 28: 1879-1887

Fan Z, Braeuning A, Cao K, Zhu S (2009) Growth-climate responses of high-elevation conifers in the central Hengduan Mountains, southwestern China. Forest Ecol Manag 258: 306-313

Fang K, Gou X, Chen F, Li J, D'Arrigo R, Cook E, Yang T, Davi N (2010) Reconstructed droughts for the southeastern Tibetan Plateau over the past 568 years and its linkages to the Pacific and Atlantic Ocean climate variability. Clim Dynam 35: 577-585

Flexas J, Medrano H (2002) Drought-inhibition of photosynthesis in C-3 plants: Stomatal and non-stomatal limitations revisited. Ann Bot-London 89: 183-189

Fritts HC (1976) Tree Rings and Climate. London, New York and San Francisco: Academic Press

Hall A, Manabe S (1999) The role of water vapor feedback in unperturbed climate variability and global warming. J Clim 12: 2327-2346

Held IM, Soden BJ (2000) Water vapor feedback and global warming. Annu Rev Environ Resour 25: 441-475

Held IM, Soden BJ (2006) Robust responses of the hydrological cycle to global warming. J Clim 19: 5686-5699

Huang R, Zhu H, Liu X, Liang E, Griessinger J, Wu G, Li X, Brauning A (2017) Does increasing intrinsic water use efficiency (iWUE) stimulate tree growth at natural alpine timberline on the southeastern Tibetan Plateau? Global Planet Change 148: 217-226

610 Huntington TG (2006) Evidence for intensification of the global water cycle: Review and synthesis. J
611 Hydrol 319: 83-95
612 Krishnamurthy L, Krishnamurthy V (2014a) Decadal scale oscillations and trend in the Indian monsoon
613 rainfall. Clim Dynam 43: 319-331
614 Krishnamurthy L, Krishnamurthy V (2014b) Influence of PDO on South Asian summer monsoon and
615 monsoon-ENSO relation. Clim Dynam 42: 2397-2410
616 Krishnamurthy V, Goswami BN (2000) Indian monsoon-ENSO relationship on interdecadal timescale.
617 J Clim 13: 579-595
618 Krishnan R, Sugi M (2003) Pacific decadal oscillation and variability of the Indian summer monsoon
619 rainfall. Clim Dynam 21: 233-242
620 Laine A, Nakamura H, Nishii K, Miyasaka T (2014) A diagnostic study of future evaporation changes
621 projected in CMIP5 climate models. Clim Dynam 42: 2745-2761
622 Lawlor DW, Cornic G (2002) Photosynthetic carbon assimilation and associated metabolism in relation
623 to water deficits in higher plants. Plant Cell Environ 25: 275-294
624 Li J, Shi J, Zhang DD, Yang B, Fang K, Yue PH (2017) Moisture increase in response to high-altitude
625 warming evidenced by tree-rings on the southeastern Tibetan Plateau. Clim Dynam 48: 649-660
626 Liang EY, Shao XM, Xu Y (2009) Tree-ring evidence of recent abnormal warming on the southeast
627 Tibetan Plateau. Theor Appl Climatol 98: 9-18
628 Liu J, Yang B, Qin C (2011) Tree-ring based annual precipitation reconstruction since AD 1480 in south
629 central Tibet. Quatern Int 236: 75-81
630 Liu J, Nina D (2015) Tree-ring recorded 644-year precipitation variations on the southwestern Tibetan
631 Plateau. Quatern Sci 35: 1082-1092
632 Liu X, Zeng X, Leavitt SW, Wang W, An W, Xu G, Sun W, Wang Y, Qin D, Ren J (2013) A 400-year
633 tree-ring delta O-18 chronology for the southeastern Tibetan Plateau: Implications for inferring
634 variations of the regional hydroclimate. Global Planet Change 104: 23-33
635 Liu Y, An ZS, Linderholm HW, Chen DL, Song HM, Cai QF, Sun JY, Tian H (2009) Annual
636 temperatures during the last 2485 years in the mid-eastern Tibetan Plateau inferred from tree rings.
637 Sci China Ser D Earth Sci 52: 348-359
638 Masson-Delmotte V, Schulz M, Abe-Ouchi A, Beer J, Ganopolski A, González Rouco JF, Jansen E,
639 Lambeck K, Luterbacher J, Naish T, Osborn T, Otto-Bliesner B, Quinn T, Ramesh R, Rojas M, Shao
640 X, Timmermann A (2013) Information from paleoclimate archives. In: Stocker TF, Qin D, Plattner
641 GK, Tignor M, Allen SK, Boschung J, Nauels A, Xia Y, Bex V, Midgley PM (eds) Climate change
642 2013: the physical science basis. Contribution of working group I to the ffth assessment report of the
643 intergovernmental panel on climate change. Cambridge University Press, Cambridge
644 Melvin TM, Briffa KR (2008) A "signal-free" approach to dendroclimatic standardisation.
645 Dendrochronologia 26: 71-86
646 Melvin TM, Briffa KR (2014a) CRUST: Software for the implementation of Regional Chronology
647 Standardisation: Part 1. Signal-Free RCS. Dendrochronologia 32: 7-20
648 Melvin TM, Briffa KR (2014b) CRUST: Software for the implementation of Regional Chronology
649 Standardisation: Part 2. Further RCS options and recommendations. Dendrochronologia 32: 343-356
650 Michaels HJ, Benner B, Hartgerink AP, Lee TD, Rice S, Willson MF, Bertin R (1988) Seed size variation:
651 magnitude, distribution, and ecological correlates. Evol Ecol 2: 157-166
652 Oren R, Sperry JS, Katul GG, Pataki DE, Ewers BE, Phillips N, Schafer K (1999) Survey and synthesis
653 of intra- and interspecific variation in stomatal sensitivity to vapour pressure deficit. Plant Cell

654 Environ 22: 1515-1526
655 Qin J, Yang K, Liang S, Guo X (2009) The altitudinal dependence of recent rapid warming over the
656 Tibetan Plateau. Clim Change 97: 321-327
657 Ryan MG, Bond BJ, Law BE, Hubbard RM, Woodruff D, Cienciala E, Kucera J (2000) Transpiration
658 and whole-tree conductance in ponderosa pine trees of different heights. Oecologia 124: 553-560
659 Sabade SS, Kulkarni A, Kripalani RH (2011) Projected changes in South Asian summer monsoon by
660 multi-model global warming experiments. Theor Appl Climatol 103: 543-565
661 Sabeerali CT, Rao SA, Dhakate AR, Salunke K, Goswami BN (2015) Why ensemble mean projection
662 of south Asian monsoon rainfall by CMIP5 models is not reliable? Clim Dynam 45: 161-174
663 Sherwood SC, Meyer CL (2006) The general circulation and robust relative humidity. J Clim 19: 6278-
664 6290
665 Sherwood SC, Ingram W, Tsushima Y, Satoh M, Roberts M, Vidale PL, O'Gorman PA (2010) Relative
666 humidity changes in a warmer climate. J Geophys Res Atmos: 115. 10.1029/2009JD012585
667 Shi C, Daux V, Zhang QB, Risi C, Hou SG, Stievenard M, Pierre M, Li Z, Masson-Delmotte V (2012)
668 Reconstruction of southeast Tibetan Plateau summer climate using tree ring delta O-18: moisture
669 variability over the past two centuries. Clim Past 8: 205-213
670 Shi C, Masson-Delmotte V, Daux V, Li Z, Carre M, Moore JC (2015) Unprecedented recent warming
671 rate and temperature variability over the east Tibetan Plateau inferred from Alpine treeline
672 dendrochronology. Clim Dynam 45: 1367-1380
673 Shi CM, Masson-Delmotte V, Daux V, Li ZS, Zhang QB (2010) An unstable tree-growth response to
674 climate in two 500 year chronologies, North Eastern Qinghai-Tibetan Plateau. Dendrochronologia 28:
675 225-237
676 Sooraj KP, Terray P, Mujumdar M (2015) Global warming and the weakening of the Asian summer
677 monsoon circulation: assessments from the CMIP5 models. Clim Dynam 45: 233-252
678 Sun Y, Ding Y (2011) Responses of South and East Asian summer monsoons to different land-sea
679 temperature increases under a warming scenario. Chinese Sci Bull 56: 2718-2726
680 Turner AG, Annamalai H (2012) Climate change and the South Asian summer monsoon. Nat Clim
681 Change 2: 587-595
682 Wang J, Yang B, Qin C, Kang S, He M, Wang Z (2014) Tree-ring inferred annual mean temperature
683 variations on the southeastern Tibetan Plateau during the last millennium and their relationships with
684 the Atlantic Multidecadal Oscillation. Clim Dynam 43: 627-640
685 Wang J, Yang B, Ljungqvist FC (2015) A Millennial Summer Temperature Reconstruction for the
686 Eastern Tibetan Plateau from Tree-Ring Width. J Clim 28: 5289-5304
687 Wentz FJ, Ricciardulli L, Hilburn K, Mears C (2007) How much more rain will global warming bring?
688 Science 317: 233-235
689 Wernicke J, Griessinger J, Hochreuther P, Braeuning A (2015) Variability of summer humidity during
690 the past 800 years on the eastern Tibetan Plateau inferred from delta O-18 of tree-ring cellulose. Clim
691 Past 11: 327-337
692 Wernicke J, Hochreuther P, Griessinger J, Zhu H, Wang L, Braeuning A (2017) Multi-century humidity
693 reconstructions from the southeastern Tibetan Plateau inferred from tree-ring delta O-18. Global
694 Planet Change 149: 26-35
695 Wilson R, Anchukaitis K, Briffa KR, Buentgen U, Cook E, D'Arrigo R, Davi N, Esper J, Frank D,
696 Gunnarson B, Hegerl G, Helama S, Klesse S, Krusic PJ, Linderholm HW, Myglan V, Osborn TJ,
697 Rydval M, Schneider L, Schurer A, Wiles G, Zhang P, Zorita E (2016) Last millennium northern

698 hemisphere summer temperatures from tree rings: Part I: The long term context. Quatern Sci Rev 134:
699 1-18
700 Xu H, Hong Y, Hong B (2012) Decreasing Asian summer monsoon intensity after 1860 AD in the global
701 warming epoch. Clim Dynam 39: 2079-2088
702 Yang B, Qin C, Wang J, He M, Melvin TM, Osborn TJ, Briffa KR (2014) A 3,500-year tree-ring record
703 of annual precipitation on the northeastern Tibetan Plateau. P Natl Acad Sci Usa 111: 2903-2908
704 Zhang X, Zwiers FW, Hegerl GC, Lambert FH, Gillett NP, Solomon S, Stott PA, Nozawa T (2007)
705 Detection of human influence on twentieth-century precipitation trends. Nature 448: 461-464